Physical and high-temperature permeation features of double-layered cellular filtering membranes prepared via freeze casting of emulsified powder suspensions

Suelen Barg[a,*], Murilo D.M. Innocentini[b], Rodolfo V. Meloni[b], Welton S. Chacon[b], Hailing Wang[c], Dietmar Koch[c], Georg Grathwohl[c]

[a] *Center for Advanced Structural Ceramics, Department of Materials, Imperial College, SW7 2AZ London, UK*
[b] *Chemical Engineering Course, University of Ribeirão Preto, 14096-900 Ribeirão Preto, Brazil*
[c] *Keramische Werkstoffe und Bauteile, University of Bremen, D-28359 Bremen, Germany*

1. Introduction

High-performance cellular ceramics with controlled pore size are attractive materials for several solid–fluid separation applications. A structure that minimizes the pressure drop and enhances fluid mixing and contact area is especially interesting for the development of membranes for removal of contaminants and separation of suspended particles from gaseous and liquid suspensions [1–3].

Regardless the configuration of the filtration module (tube, disc or plate) or the features of the porous structure (granular, fibrous or cellular), ceramic membranes must meet several performance criteria to ensure their acceptability in the market. Permeability and dust separation efficiency are two key indicators that ultimately determine the service life of membranes for aerosol filtration in environmental control and pollution abatement processes [3,4].

Permeability helps to quantify the required power to force the gas to percolate the filtering membrane in an economical rate, whereas separation efficiency indicates the ability to meet atmospheric or indoor particulate emission regulations [4–6].

The particle collection in aerosol filters should preferentially occur at the external membrane surface, on which a dust layer (cake) is continuously deposited and periodically removed, so the residual pressure drop is kept within acceptable levels. The penetration of particles inside the membrane may result in progressive clogging of pores and irreversible reduction of the operational flow rate. On the other hand, if properly designed and operated, the membrane may have both its permeability and separation efficiency kept within satisfactory and stable levels during a great number of filtering–cleaning cycles [3,6].

The superficial membrane features play an important role on the aerosol filtration performance. Compared with other collection mechanisms, the membrane acts primarily as a physical barrier that separate fluid and particles [7]. A superficial layer of small pores is thus advantageous for particle collection and cake detachment. If such a filtering layer is made thin and supported by a matrix containing larger pores, then both acceptable pressure drop and mechanical integrity can be achieved in a single composite structure.

Previous attempts for the development of such composite membranes have included the deposition of a thin particle-bonded layer on the top of a ceramic foam support [5,8]. Support layers are

* Corresponding author. Tel.: +44 (0) 7837748898.
E-mail address: suelen.barg@imperial.ac.uk (S. Barg).

normally produced by the replica technique, in which both porosity and pore size are pre-determined by the polymeric matrices [1]. The filtering layer is produced by the deposition of a thin coating over the support layer [9,10]. In this case, the pore size is controlled by the composition of pastes that include ceramic particles and binders. The main drawbacks of this processing route are the poor adherence between both layers and the fact that due to differences in physical properties, the mechanical and thermal stress caused by successive filtration/cleaning cycles may damage and detach the filtering layer, with loss of filter efficiency [8].

A promising approach to achieve all the advantages of double-layered filtering membranes, and subject of this work, is the development of cellular ceramics of graded porosity and pore size. Recently, a versatile direct foaming method has been developed, in which a water immiscible alkane phase is emulsified in an aqueous inorganic powder suspension, giving rise to cellular structures presenting excellent mechanical properties due to the defect-free struts and particularly tailored microstructural features as highly interconnected cells [11–17]. Furthermore, this technique allows the formation of layers of stable emulsions with individual porosity parameters leading to graded structures of self assembled open porous interfaces. Graded structures presenting compressive strength of 24 MPa for 79% porosity could be produced [13].

If a low concentration of alkane droplets is emulsified in the aqueous powder suspension, a low alkane phase emulsified suspension (LAPES) is formed [11], while high concentration of droplets results in the so called high alkane phase emulsified suspensions (HAPES) [12]. In LAPES, foaming (which is provided by the evaporation of the alkane droplets) can lead to a time-dependent expansion of the emerging foam resulting in the controlled formation of microstructures with cell sizes averaging in the mm scale (0.3–4 mm). In HAPES, the high concentration of droplets acts against the foam growth resulting in cell sizes in the low micrometric scale (3–200 μm). The emulsified suspensions can be simple consolidated by the controlled expansion of the alkane droplets due to foaming and concurrent drying. Alternatively, freeze gelation/casting techniques are applied as further means to achieve new types of porous microstructures, overcoming some geometrical restrictions and accelerating the process [14].

The objective of this project is the development of alumina double-layered membranes via freeze casting of HAPES and the evaluation of their permeability as a function of temperature. The processing technique relies on the freezing, freeze drying and subsequent sintering of combined HAPES layers with adjusted porosity parameters and thickness. Freeze casting was adopted as consolidation method of the green foams resulting in minimal shrinkage during freeze drying. This step overcomes the geometrical restrictions normally happening due to cracks formation during drying. Consequently, graded filters with open porosity throughout the adjacent layers can be produced. In this paper, the process is described and permeation performance and the physical features of the produced membranes are presented. Airflow tests were conducted from ambient temperature up to 415 °C in order to evaluate the sensitivity of the permeability coefficients under typical industrial operation. The implications for hot aerosol filtration performance are discussed.

2. Experimental procedure

2.1. Double-layered membranes preparation

For the processing of the double-layered membranes, high alkane phase emulsified alumina suspensions (alumina-HAPES) with controlled microstructures were produced. For this, initially a stabilized alumina powder suspension was prepared by the slow addition of alumina powder (Alcoa CT 3000 SG) with an average particle diameter (d_{50}) of 500 nm and a specific surface area of 7.5 $m^2\,g^{-1}$ into deionized water containing Dolapix CE–64 (0.74 wt% related to alumina) as negatively charged electrosteric dispersion agent. The suspensions were dispersed and homogenized for 20 min in a laboratory mixer (Dispermat LC, VMA Getzmann GmbH) at a mixing velocity of 2500 rpm. Further on starch was added as binder (1.5–3 wt% to alumina) and the suspensions were further mixed for 5 min in a water bath at 50 °C. The alumina suspensions with a particle content of 42 vol% were subjected to de-aeration to remove undesired entrapped bubbles under reduced pressure (5 kPa). Finally, the continuous phase is heated up to 65 °C to ensure gelling of the starch.

Alumina-HAPES were prepared by emulsifying 65 vol% decane ($C_{10}H_{22}$) from Fluka (hydrophobic dispersed phase) into alumina aqueous suspensions (continuous phase) with the addition of sodium lauryl sulphate (SLS) (BASF, Lutensid AS 2230) as anionic surfactant (between 0.11 and 0.22 vol%, depending on the employed stirring rate) and mechanical stirring as emulsification effect. To ensure the stability of the system, the anionic surfactant was used under alkaline conditions (pH = 9.5), where the strong negative zeta potential of the alumina suspensions was provided by the dispersion agent [11]. Emulsification was undertaken under reduced pressure (10 kPa) and room temperature to avoid the abundant incorporation of air bubbles and also to prevent evaporation of decane, which has a vapor pressure of 0.19 kPa at 25 °C.

It is very important to control the alkane droplets size in HAPES due to their strong influence on the cell and window size and consequently on the permeability of the emerging open porous structures. The emulsification stirring velocity is a decisive parameter for the control of droplets size in HAPES, since with the increase of the stirring velocity the shear stress acting on the droplets during emulsification increases, resulting in smaller droplets and cells sizes [12]. Emulsification of HAPES was undertaken at 800 rpm and 2000 rpm during 2 min for the production of the support and filtering layers, respectively. Furthermore, the stability of green bodies increases at higher droplets concentration; emulsification of 65 vol% decane under 800 rpm leads then to less concentrated larger droplets and a larger amount of starch as binder is added (3 wt% to alumina in suspension) ensuring green foams integrity.

For the production of the double-layered membranes, the alumina-HAPES emulsified under 800 rpm was cast in an aluminum mold (34 mm diameter × 15 mm height). A doctor blade process was then applied moving the blade along the surface of the filled mold to ensure the removal of excess HAPES and provide a precise shaping of the green foam, keeping the upper surface open to the atmosphere. Subsequently, the same procedure was repeated applying slightly higher wall segments (2 mm) and a second casting step with HAPES emulsified at 2000 rpm. Since the secondary HAPES differed in its emulsification parameters from the first one, a change in the cell size between the first and the second layer was achieved. The successful realization of cell size gradients with interconnecting interfaces has to take into account the time of successive casting, the viscosity of the subsequent layer and the consolidation method [13].

To ensure a precise shaping, the molded samples were frozen at −150 °C for 30 min. The frozen samples were de-molded and directly placed at a conventional freeze dryer at −20 °C. As decane is liquid under these conditions (melting point at −27.5 °C), it can be easily removed from the frozen parts by the reduction of the pressure in the freeze dryer. The samples were consolidated by the subsequent sublimation of water. The freeze drying step is very important to exclude any crack formation associated to drying and evaporation of the large amount of decane. Complete freeze drying of the foams was achieved during 14 h. After de-molding, the

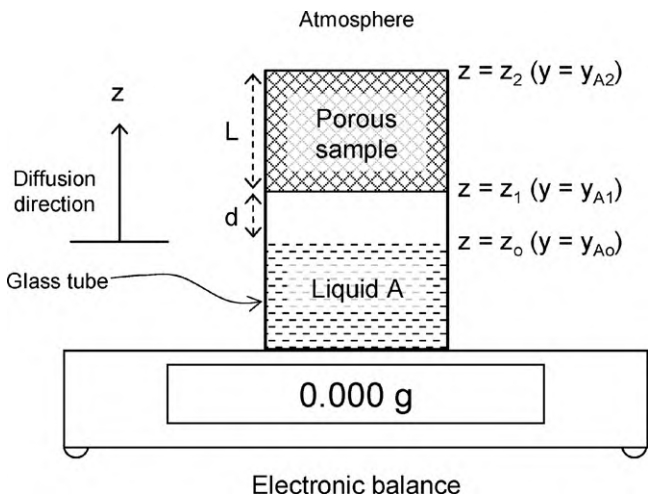

Fig. 1. Schematic of diffusion cell used for tortuosity evaluation.

shaped green alumina membranes were sintered at 1550 °C for 2 h with heating and cooling rates of 2 K/min and 5 K/min, respectively.

2.2. Characterization of the cellular structure

The samples were physically characterized with regard to their cell size, porosity, thermal expansion, tortuosity and permeability. The microstructure and morphology of samples were analyzed by Scanning Electron Microscopy, SEM (Camscan 24). Cell sizes were measured from planar sections of embedded samples with the linear intercept method using the software Linear Intercept (TU Darmstadt). The average cell sizes, d_{50}, d_{10} and d_{90}, were determined from the cumulative cell size distribution curves. The linear expansion of the sintered samples as a function of temperature was measured via dilatometry (TMA 80lS, Bähr Thermoanalyse GmbH).

The density of the solid fraction (ρ_s), the bulk density (ρ_b) and open porosity (ε) were evaluated by mass and geometric measurements and by the water displacement method (Archimedean principle). Samples were kept in water for 30 min under vacuum prior to the wet and immerse weight measurements. This non-destructive method allows to account the volume of open pores, being effective as fluid transport paths.

Tortuosity was evaluated by the determination of the effective diffusivity of a vapor within the sample in an adapted Arnold diffusion cell shown in Fig. 1 [18]. A chamber is partially filled with a pure liquid A that evaporates into a stagnant phase of an inert gas B (air) and diffuses upward through the porous sample. The gas-phase concentration of component A is in equilibrium with its liquid phase at the interface. The whole system is presumed to be held at constant temperature T and pressure P and therefore the gas diffusivity D_{AB} is considered constant.

The following hypotheses were considered [19,20]: (a) the gas mixture is ideal; (b) gas B has negligible solubility in liquid A; (c) the gas concentration of A at the upper surface of the sample ($z = z2$) is null due to natural flux of gas B (air) pure; (d) there is no chemical reaction in the system; (e) diffusion occurs only through open pores, with negligible adsorption of vapor A on the pore walls or Knudsen diffusion into them; (f) both vaporization and diffusion occur in a quasi-steady state in the z direction only (Fig. 1). Based on this set of hypotheses, the rate of vaporization of liquid A was mathematically expressed in terms of the molar mass flux N_{Az} [mol m^{-2} s^{-1}], and obtained by the integration of the equation of continuity coupled with Fick's law of diffusion:

$$N_{Az} = \frac{cD_{eff}}{L} \ln\left(\frac{1}{1 - y_{A1}}\right) \tag{1}$$

in which c is the total molar concentration of species A and B in the gaseous mixture [mol m^{-3}], D_{eff} is the effective diffusivity of vapor A inside the sample [m^2 s^{-1}], L is the sample thickness [m] and y_{A1} is the molar fraction of gas A at the bottom surface of the sample [mol/mol].

The effective diffusion coefficient (D_{eff}) in Eq. (1) is numerically smaller than the diffusion coefficient of gaseous mixture molecules in the absence of the porous media (D_{AB}). This is because bulk diffusion is hindered by the pore walls. Therefore, the effective diffusivity D_{eff} is coupled to D_{AB} by:

$$D_{eff} = \frac{\varepsilon}{\tau} D_{AB} \tag{2}$$

in which ε is the open porosity of the medium and τ is the tortuosity, defined as the ratio of the actual diffusion path length per unit length of the medium. Both ε and τ are dimensionless and D_{eff} has the same units of D_{AB} [m^2 s^{-1}].

On the other hand, the molar flux (N_{Az}) mathematically derived in Eq. (1) can also be obtained from the experimental set-up from:

$$N_{Az} = \frac{\Delta m}{\Delta t S M_A} \tag{3}$$

in which Δm [kg] is the mass variation measured during the testing time Δt [s], S is the cross-sectional sample surface exposed to vapor diffusion [m^2] and M_A is the molar mass of the gas A [kg mol^{-1}].

The tortuosity of the medium can be obtained from the set of Eqs. (1)–(3). For this work, n-hexane (molar mass = 86.17 g mol^{-1}) was used as evaporating liquid A in the diffusion experiments run at ambient conditions. The mass loss curve during each test was computer-recorded at 0.15 s intervals for at least 600 s. The gas-phase diffusion coefficient for n-hexane was previously measured in an original Arnold diffusion cell ($D_{AB} = 1.06 \times 10^{-5}$ m^2 s^{-1} at 26.7 °C) and corrected for the actual absolute atmospheric pressure P_{atm} and temperature T of each test ($P_{atm} \cong 95059$ Pa and $T \cong 26$–27 °C). For reproducibility purposes, three samples were tested for tortuosity and for each one three mass loss curves were experimentally obtained. Sample surface exposed to diffusion (S) was kept in 6.83 cm^2.

The evaluation of the permeability was based on Forchheimer's equation, an empirical relationship well accepted in the literature to express the parabolic dependence of pressure drop (ΔP) through the flat medium with the resulting superficial or face velocity (v_s) of the fluid [21–24]:

$$\frac{\Delta P}{L} = \frac{\mu}{k_1} v_s + \frac{\rho}{k_2} {v_s}^2 \tag{4}$$

For compressible flow of gases and vapors, ΔP can be calculated from:

$$\Delta P = \frac{{P_i}^2 - {P_o}^2}{2P} \tag{5}$$

in which P_i and P_o are, respectively, the absolute fluid pressures at the entrance and exit of the medium [Pa], L is the medium length or thickness along the macroscopic flow direction [m], μ is the fluid viscosity [Pa s] and ρ is the fluid density [kg m^{-3}]. The superficial or face velocity v_s is the volumetric flow rate Q [m^3 s^{-1}] divided by the nominal face area of the sample exposed to flow, A_{flow} [m^2]. P is the absolute pressure (either P_i or P_o) for which v_s, μ and ρ are determined. In this work, P_o and T_o were considered as reference conditions to obtain v_s, μ and ρ.

The effect of the porous structure in Eq. (4) is quantified by the thickness L and the permeability parameters k_1 and k_2, which are complex functions of the morphology, size distribution, connectivity and volume of the void fraction [23–25]. Usually, these parameters are referred to as permeability coefficients, which are

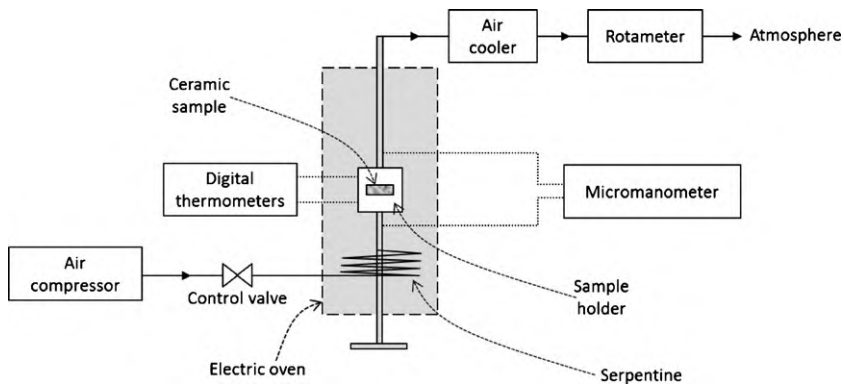

Fig. 2. Schematic of apparatus used for hot air permeation tests.

supposed to be independent of the body dimensions and of both fluid and flow conditions, even though they may vary with temperature. The terms k_1 and k_2 are also known as Darcian and non-Darcian permeability coefficients or constants, in reference to Darcy's law, which establishes a linear dependence between pressure drop and fluid velocity [23–25].

In this work, the experimental evaluation of permeability was carried out in temperatures ranging from 20 to 415 °C. In these tests air was forced to flow through the porous sample in stationary regime. The sample was laterally sealed between two 316L stainless steel chambers and flow was controlled by a needle valve. Pressures P_i and P_o were measured by a digital micromanometer (Gulpress 200, Instrutemp) and recorded as a function of the air volumetric flow rate Q, measured with rotameters (0–40 L min^{-1}) and soap-bubble flow meters (0–10 L min^{-1}) and converted to the superficial velocity by $v_s = Q/A_{flow}$. The whole system (chambers and sample-holder) was set within an electric furnace (7500 W) controlled by a PID system, to realize various temperature–time programs. Air was pre-heated in a 2 m-long 316 stainless steel serpentine within the furnace chamber before reaching the sample. Temperature was measured with K-type thermocouples situated perpendicular to the sample at the entrance and exit chambers. Thermocouples were also used to monitor the air temperature near the pressure transducers and prior to entering in the flowmeter devices. The air temperature (T_o) and pressure (P_o) measured at the outlet stream were applied for calculations of air density and viscosity. Fig. 2 shows a schematic of the hot air permeameter (HAP) employed in the tests.

In the tests, firstly the sample (flat disk with ≅3 cm of diameter and 8–9 mm of thickness) was tightly fixed in the sample-holder using heat-resistant O-rings to avoid leakage. The temperature was raised to the desired point and air allowed to flow upwards through the sample with a constant pressure P_i. When the steady-state regime was reached (constant T, P_i and P_o), the volumetric flow rate Q was measured at the sample exit. Three flow rate measurements were carried out for each pressure setting at a given temperature. After the collection of at least 10 pairs of pressure and flow rate data, the temperature was raised and the whole procedure repeated. The collected data set was treated according to the least-square method using a parabolic model of the type: $y = ax + bx^2$, in which y was $\Delta P/L$ and x was the air velocity v_s. The permeability parameters of Forchheimer's equation (Eq. (4)) were then calculated from the fitted constants a and b respectively by $k_1 = \mu/a$ and $k_2 = \rho/b$. For permeability evaluation, three samples were tested at room temperature only and other two samples were subjected to hot air flow.

Changes in fluid properties were also considered for the evaluation of permeability coefficients. Both air density (ρ) and air viscosity (μ) were calculated based on the temperature (T_o) and pressure (P_o) at the exit stream according to the following equations [23]:

$$\rho = \frac{P_o MM_{air}}{RT_o} \tag{6}$$

$$\mu = 1.73 \times 10^{-5} \left(\frac{T_o}{273}\right)^{1.5} \left(\frac{398}{T_o + 125}\right) \tag{7}$$

in which MM_{air} is the average molar mass of dry air (28.965×10^{-3} kg mol^{-1}) and R is the ideal gas constant (8.314 Pa m^3 mol^{-1} K^{-1}).

An equivalent transport pore diameter d_{transp} was obtained for the tested samples from permeability and tortuosity data. This approach is very common to predict equivalent pore sizes in soils and basically involves the coupling of permeation and diffusion models [26]. For instance, considering the pores as a network of tortuous tubes of different diameters, Ficks' law for diffusive transport can be combined with Poiseuille's law for convective fluid transport. The following relationship results then for the equivalent transport pore diameter (d_{transp}) [18,26]:

$$d_{transp} = \left(\frac{32k_1}{\varepsilon/\tau}\right)^{0.5} \tag{8}$$

Eq. (8) includes only bulk features and for this reason is expected to provide an average value for the whole structure. The range of validity for this equation is within the viscous flow regime, where the influence of k_1 predominates [18].

3. Results and discussion

The typical microstructure of a sintered double-layered membrane produced in this work is shown in Fig. 3. The HAPES droplet size and consequently the cell size distribution of the membrane layers were efficiently controlled by the emulsification stirring rate. The membranes experienced a 13% linear shrinkage during sintering. A reduction in the average cell size (d_{50}) from 13 to 5.5 μm was observed when HAPES were emulsified under 800 rpm (support layer) and 2000 rpm (filtering layer), respectively. Furthermore, with increasing stirring rate narrower cell size distributions were realized (Fig. 4).

Table 1 summarizes the average physical and permeation features of membranes obtained at room temperature. The porous structures were characterized by highly interconnected cells, with high open porosities (77.4% ± 0.1%). Pycnometry tests also confirmed both the skeletal density (3944.6 ± 47.7 kg m^{-3}) and bulk density (891.9 ± 14.8 kg m^{-3}) of the samples. Permeation tests with airflow at room temperature resulted in average values for

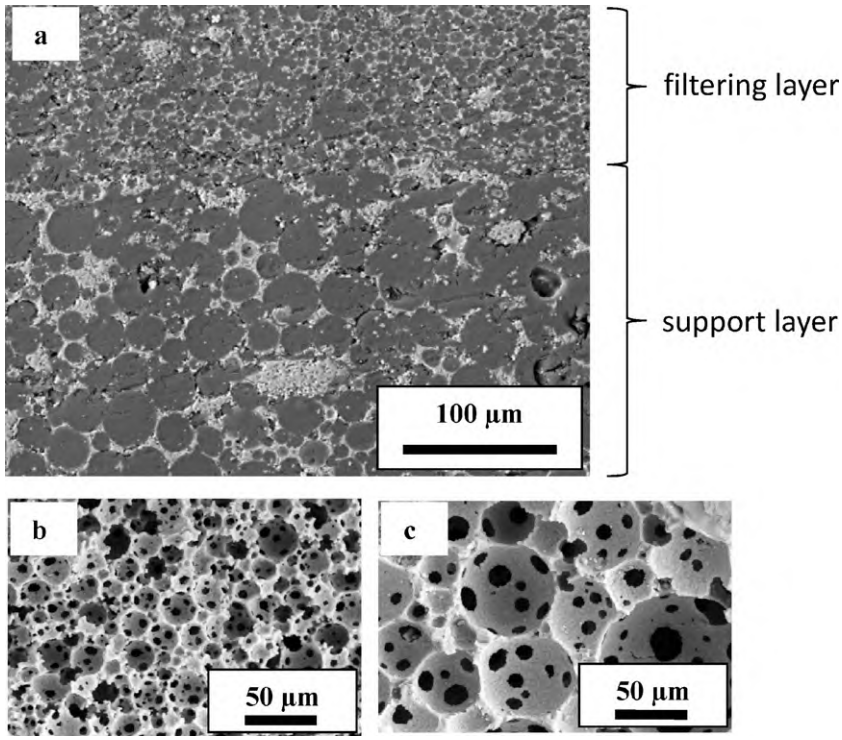

Fig. 3. SEM micrographs of double-layered membranes produced by freeze casting of HAPES emulsified under 800 rpm (support layer) and 2000 rpm (filtering layer). (a) Embedded double-layered membranes (dark phase corresponds to embedding polymer). (b) Detail of fracture surface of filtering layer. (c) Detail of fracture surface of support layer.

Table 1
Physical and fluid dynamic parameters obtained at room temperature for the double-layered membranes.[a]

Properties	ρ_s (kg m^{-3})	ρ_b (kg m^{-3})	ε	τ	k_1 (10^{-12} m^2)	k_2 (10^{-6} m)	d_{transp} (µm)
Average	3944.6	891.9	0.774	2.24	2.09	1.80	13.9
Deviation	47.7	14.8	0.001	0.08	0.47	0.52	1.7

[a] Values refer to the room temperature tests carried out with 3 samples.

k_1 and k_2 coefficients respectively of $2.09 \pm 0.47 \times 10^{-12}$ m^2 and $1.80 \pm 0.52 \times 10^{-6}$ m.

Typical mass loss curves obtained in the gas diffusion experiments are shown in Fig. 5. The excellent linearity of curves indicate that the molar flux N_{Az} was constant during the testing time, an important hypothesis for validation of equations used for tortuosity assessment. The average tortuosity for the three samples tested in triplicate was 2.24 ± 0.08. Based on the k_1, ε and τ values, an average equivalent transport pore diameter (d_{transp}) was calculated, with a value of 13.9 µm, very close to the average size (d_{50}) of the support layer obtained by conventional optical analysis.

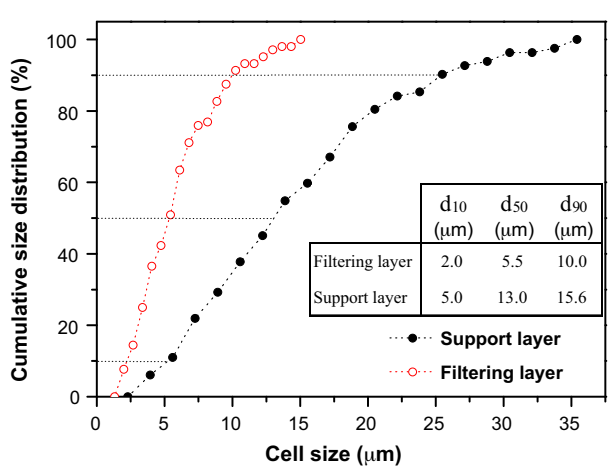

Fig. 4. Cumulative cell size distribution of filtering layer and support layer produced from HAPES emulsified under 2000 and 800 rpm, respectively.

These microstructural studies make clear that the solid phase (strut, matrix, etc.) is characterized by a very high relative density revealing no considerable micro porosity or enclosed pores. The continuous transition and perfect interjunction between the support and filtering layers is also manifested in Fig. 3.

Permeation curves as function of temperature are shown in Fig. 6. Pressure drop increased with the increase in air velocity, following clear parabolic trend in all cases, which confirmed that Forchheimer's equation fitted better to experimental data than the pure linear relationship stated by Darcy's law [23].

The increase in air temperature also shifted the pressure drop to higher values and this behavior is related to changes in both fluid and medium properties. On one side, density and viscosity of the gas phase are oppositely affected by temperature. In the tested temperature range of 20–415 °C, Eqs. (6) and (7) predict a reduction of ~58% in air density ρ and an increase of ~85% in air viscosity μ, which affects in the same proportions the intensities of the quadratic-inertial $[\rho v_s^2/k_2]$ and the linear-viscous $[\mu v_s/k_1]$ terms of Eq. (4), respectively. The predominant effect of these changes on the sample pressure drop will depend on the velocity applied. In the range of 1–5 cm/s (typical for hot gas filtration), the pressure

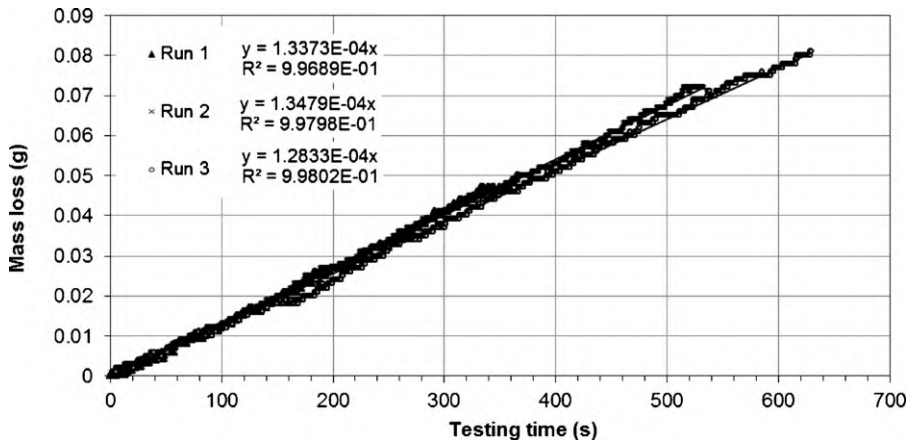

Fig. 5. Typical mass loss curves obtained during the gas diffusion-tortuosity experiments.

drop of tested membranes at room temperature was about 98% due to viscous effects and only 2% due to inertia, so the increase in viscosity is expected to have much greater influence on pressure drop than the reduction in air density.

Fig. 7 shows that permeability coefficients k_1 and k_2 of the double-layered membrane were also affected the temperature increase. Opposite but consistent trends were observed for the permeability coefficients, with an average 24% increase for k_1 and 94% decrease for k_2. For this latter coefficient, the major decrease was observed from 20 to 100 °C, and then an almost constant trend up to 415 °C.

Since samples were previously sintered at 1550 °C for 2 h, such changes up to 415 °C can be assumed as reversible and related to thermal expansion effects. Fig. 8 confirms that a 0.25% linear expansion was observed in this temperature range.

Fig. 9 shows a comprehensive permeability map that classifies porous structures according to their type or application [23]. Double-layered membranes produced in this work are included in the permeability range of typical structures employed for aerosol filtration (k_1 between 10^{-13} and 10^{-9} m^2 and k_2 between 10^{-9} and 10^{-4} m), but since the average magnitudes found here were $k_1 \sim 10^{-12}$ m^2 and $k_2 \sim 10^{-6}$ m, then a further improvement in both coefficients is still possible and desirable (Fig. 10).

Permeation tests at high temperatures for finding permeability coefficients of porous ceramics are scarcely described in the literature, and for this reason only few data are available for comparison and discussion of trends [5,27]. Innocentini et al. [5] reported data for low-porosity high-alumina refractory castables previously sintered from 900 to 1650 °C and tested under airflow up to 700 °C. For samples with the highest thermal treatment temperature (1650 °C), slight increase in k_1 and decrease in k_2 with increasing test temperature were observed and also related to thermal expansion effects. In that case, the ceramic structure had

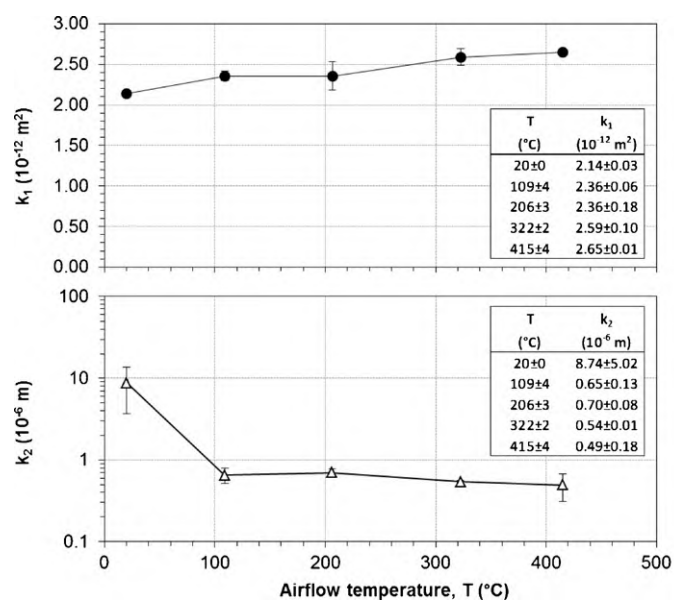

Fig. 7. Influence of airflow temperature on permeability coefficients k_1 and k_2 of double-layered membranes prepared in this work.

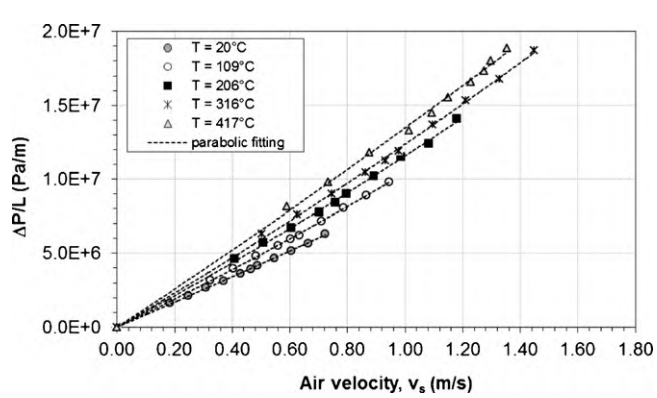

Fig. 6. Permeation curves obtained for a double-layered membrane at different airflow temperatures.

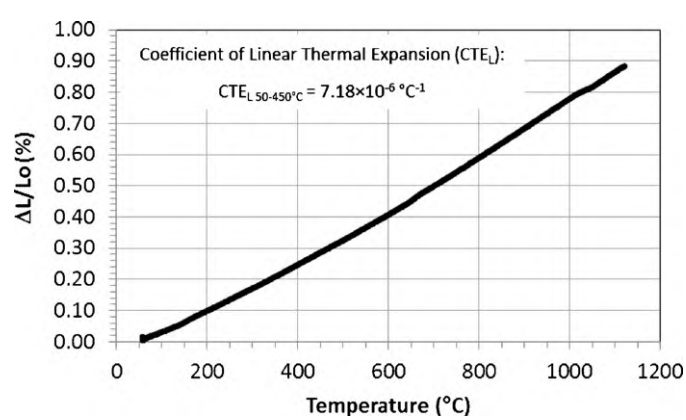

Fig. 8. Dilatometry curve for a typical double-layered membrane.

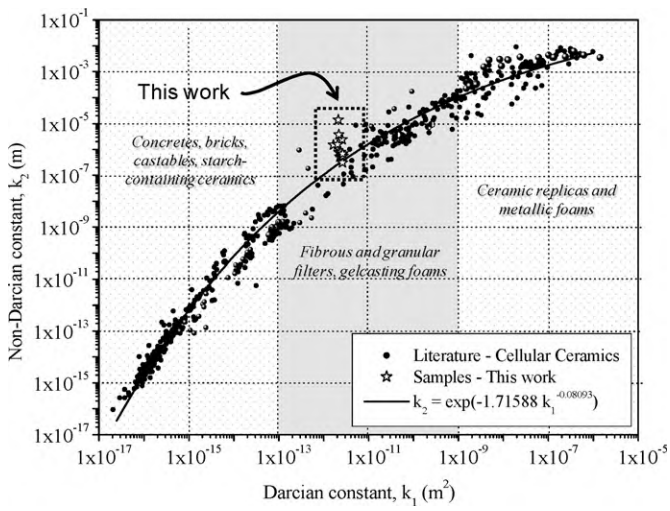

Fig. 9. Location of k_1 and k_2 data of double-layered ceramic filters in a comprehensive permeability map proposed by Innocentini et al. [23].

clearly two families of pores: small round inter-particle voids in the matrix and less tortuous large paths produced around particle aggregates due to poor packing (known as interfacial transition zone, ITZ) [28,29]. Thermal expansion acted oppositely in aperture of these pores of different morphologies and was the likely reason for the divergence of k_1 and k_2 trends. Lee and Jo [30] investigated the influence of airflow temperature on k_1 for a thin composite flat filter made of fly ash particles deposited onto a stainless steel woven mesh. These authors found an increase of k_1 from 4.8×10^{-14} to 7.1×10^{-14} m^2 (48%) for a temperature increase from 25 to 450 °C. Such increase was related to slip effects within the narrower pore channels (mean pore size of 2.3 μm and porosity of 32%). No value or trend for the k_2 coefficient with temperature was reported in that study.

The hypothesis of slip effect in high-temperature flow may not be discarded in the present work. Forchheimer's equation is based on the assumption of continuum flow. However, when the mean free path of the air (λ_{air}) becomes comparable to the pore or channel dimensions, flow is dominated by collisions of molecules with the wall, rather than by collisions between molecules and the hypothesis of continuum flow may not prevail. For this assessment, the dimensionless Knudsen number K_n can be defined as the ratio of the mean free path to the pore dimension:

$$K_n = \frac{\lambda_{air}}{d_{pore}} \tag{9}$$

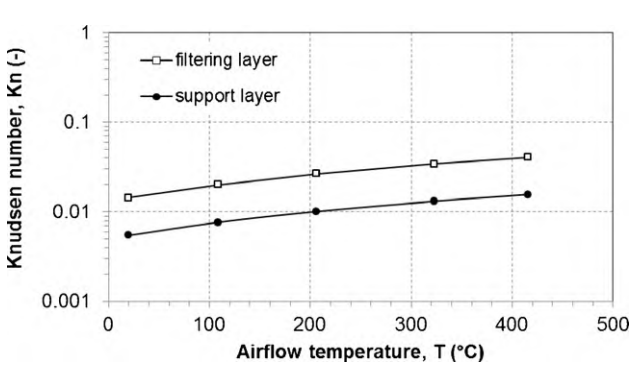

Fig. 10. Knudsen numbers calculated from Eqs. (9) to (10) for support and filtering layer in the airflow temperatures used in permeation tests.

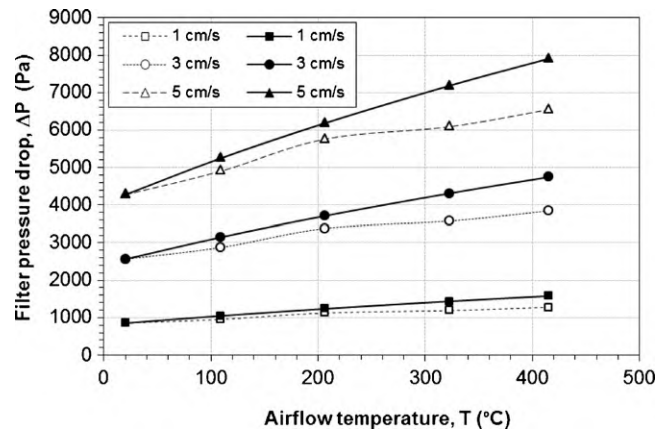

Fig. 11. Predicted pressure drops (Eqs. (4)–(7)) through 1-cm thick double-layered membranes at different temperatures and air velocities. Black symbols refer to ΔP predicted with k_1 and k_2 values obtained at 20 °C and white symbols refer to ΔP predicted with actual k_1 and k_2 values at each airflow temperature.

The mean free path of air (λ_{air}) can be computed from [31]:

$$\lambda_{air} = \left(\frac{3.2\mu}{P}\right)\left(\frac{RT}{2\pi\ MM_{air}}\right)^{0.5} \tag{10}$$

in which all units are in the International System.

Free molecular flow is characterized by $K_n > 1.0$, while continuum or non-slip flow (laminar or turbulent) is characterized by $K_n < 0.01$. Transition or slip-flow regime usually applies over the range $0.01 < K_n < 1.0$ [31].

Fig. 10 shows the trends and ranges of K_n calculated from Eqs. (9)–(10) for both support and filtering layers, based on their average pore sizes ($d_{pore} = d_{50}$), respectively of 13 μm and 5.5 μm. It is observed that K_n increases with increasing temperature and that airflow within the double-layered membrane could indeed include slip effects. So, even though the decrease in air density with temperature implied in a lower importance of the inertial term $[\rho v_s^2/k_2]$ on total pressure drop, it also increased the mean free path of air and thus changed the interaction between fluid and porous medium.

Another relevant aspect is that the casting process may have resulted in some degree of superposition of both support and filtering layers, producing an interface with singular features in terms of porosity and pore size, as reported in the literature [5,8]. As a consequence, the pressure gradient through the membrane was not uniform along its whole thickness, but changed steeply through support, interface and filtering layers. Therefore, the interpretation of trends for k_1 and k_2 obtained in this work must be careful, while a more detailed investigation is required to elucidate the influences of thermal expansion and slip flow for the double-layered membranes.

Regardless the causes, the resulting effect of changes in k_1, k_2, μ and ρ on the total membrane pressure drop at different airflow temperatures and face velocities can be observed in Fig. 11. As mentioned before, at typical filtration velocities from 1 to 5 cm/s, the viscous term $[\mu v_s/k_1]$ of Forchheimer equation is predominant. Therefore, the increase in k_1 (~24%) compensates only partially the increase of air viscosity μ (~85%) from 20 to 415 °C. The net effect shown in Fig. 11 is a slower increase in pressure drop than that expected if only the air viscosity increase were considered.

It is also worth mentioning that typical commercial filters for hot aerosol filtration are manufactured as candles, i.e., hollow-cylinder elements closed at one end and flanged in the other. Typical candle dimensions are 40–110 mm of internal diameter, 60–150 mm of external diameter and 300–3000 mm of length, with usable surface area ranging from 0.06 to 1.4 m^2/element. In this case, Forchheimer's equation to predict pressure drop must be modified

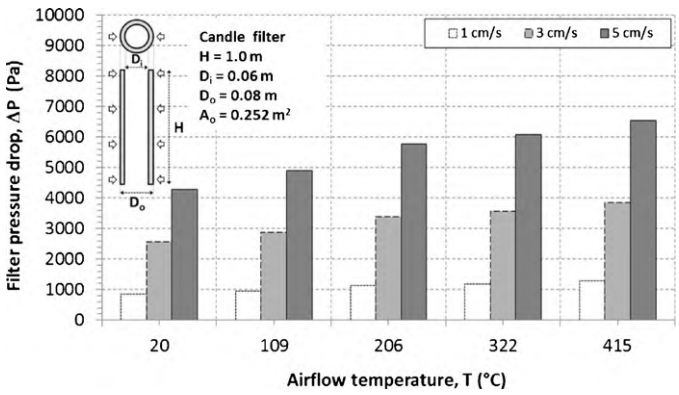

Fig. 12. Pressure drop levels predicted by Eq. (11) for a hypothetical candle filter element with composition and permeability coefficients based on the double-layered membranes prepared in this work.

to account the radial flow. The equation integrated in cylindrical coordinates becomes:

$$\frac{\Delta P}{(D_o/2)} = \frac{\mu_o}{k_1}\ln\left(\frac{D_o}{D_i}\right)v_{so} + \frac{\rho_o}{k_2}\left(\frac{D_o - D_i}{D_i}\right)v_{so}^2 \quad (11)$$

in which ΔP is given by Eq. (5), D_i and D_o are the inner and outer diameters, respectively, and μ_o, ρ_o and v_{so} are the gas viscosity, density and face velocity based on the outlet filter pressure and temperature.

Pressure drop of a virgin commercial candle filters in hot gas cleaning applications ranges typically between 400 and 8000 Pa, depending on the face velocity and type of medium (granular, metallic or fibrous) [32,33]. This pressure drop increases during the filter operation due to the deposition of the dust cake and when the value exceeds a preset value a pulse cleaning is performed. Fig. 12 shows a simulation of pressure drop for a hypothetical cylindrical filtering element with D_o = 6 cm, D_i = 4 cm, H = 100 cm, based on the ceramic composition tested in this work and the actual values of k_1 and k_2 obtained at each airflow temperature. Results showed that filter elements would have similar pressure drop performance of commercial filters up to a face velocity of 3 cm/s and temperatures up to 415 °C. Further improvement in permeability would be necessary for economic operation above 3 cm/s.

4. Conclusions

Double-layered membranes presenting favorable cell sizes, porosity and permeability values for filtration applications could be produced by the processing route based on the freeze casting of high alkane phase emulsified suspensions (HAPES). The cell size (d_{10}, d_{50}, d_{90}) could be controlled with 5, 13, 25.5 and 2, 5.5, 10 μm for support and filtering layers, respectively, by control of the stirring rate during emulsification. Permeability coefficients k_1 and k_2 were found to vary in opposite ways according to the airflow temperature, indicating different influences of thermal expansion and air slippage on the porous paths. Permeability levels for tested membranes were within the range expected for hot aerosol filters, but could be further improved in order to allow economical operation in industrial applications.

Acknowledgements

The authors would like to thank DFG for funding this project within the Research Training Group 1375 "Nonmetallic Porous Structures for Physical–Chemical Functions". Authors also thank UNAERP and MCT/CNPq/Brazil, Universal Project – Process 471814/2008-3, for the financial support.

Nomenclature

A_{flow}	face area of the membrane exposed to flow [m^2]
c	molar concentration of the gas mixture [mol m^{-3}]
D_{AB}	gas diffusivity in air [m^2 s^{-1}]
D_i	inside diameter of a hollow cylinder (candle) filter element [m]
D_o	outside diameter of a hollow cylinder (candle) filter element [m]
D_{eff}	effective gas diffusivity through the porous sample [m^2 s^{-1}]
d	distance between the gas–liquid interface and the bottom face of the sample in the diffusion test [m]
d_{20}, d_{50}, d_{90}	average cumulative pore diameters [m]
d_{pore}	average pore diameter [m]
d_{transp}	equivalent transport pore diameter [m]
H	height of cylindrical filter [m]
K_n	Knudsen number
k_1	Darcian permeability coefficient [m^2]
k_2	non-Darcian permeability coefficient [m]
L	sample thickness along the macroscopic flow direction [m]
MM_A	molar mass of diffusion gas A [mol kg^{-1}]
MM_{air}	molar mass of dry air [mol kg^{-1}]
N_{AZ}	molar flux of diffusion gas along z-direction [mol m^{-2} s^{-1}]
P	absolute fluid pressure at which v_s, μ and ρ are measured or calculated [Pa]
P_{atm}	atmospheric pressure at laboratory location [Pa]
P_i	absolute fluid pressure at the membrane entrance [Pa]
P_o	absolute fluid pressure at the membrane exit [Pa]
P_{VA}	absolute vapor pressure of diffusion gas [Pa]
Q	volumetric air flow rate [m^3 s^{-1}]
R	ideal gas constant [Pa m^3 mol^{-1} K^{-1}]
S	cross-sectional sample surface exposed to gas diffusion [m^2]
T	temperature of the fluid [K]
v_s	face or superficial fluid velocity [m/s]
z	distance in diffusion direction [m]
y	molar fraction of gas mixture [–]

Greeks

Δm	mass variation measured during the diffusion experiment [kg]
ΔP	pressure drop through the membrane [Pa]
Δt	duration of the diffusion experiment [s]
ε	porosity of the membrane
λair	mean free path of air molecules [m]
μ	absolute air viscosity [Pa s]
ρ	air density [kg m^{-3}]
ρ_b	bulk density of the membrane [kg m^{-3}]
ρ_s	density of the solid fraction [kg m^{-3}]
τ	tortuosity of the membrane

Subscripts

i	inlet or entrance of the membrane
o	outlet or exit of the membrane

References

[1] M. Scheffler, P. Colombo (Eds.), Cellular Ceramics: Structure, Manufacturing, Properties and Applications, Wiley-VCH, Weinheim, 2005.
[2] M.D.M. Innocentini, V.P. Rodrigues, R.C. Romano, R.G. Pileggi, G.M. Silva, J.R. Coury, Permeability optimization and performance evaluation of hot aerosol

filters made using foam incorporated alumina suspension, Journal of Hazardous Materials 162 (2009) 212–221.
[3] J.P.K. Seville, Gas Cleaning in Demanding Applications, Springer, 1997.
[4] C. Tien, B.V. Ramarao, Granular Filtration of Aerosols and Hydrosols, second ed., Elsevier Science and Technology Books, 2007.
[5] N. Freitas, J.A. Gonçalves, M.D.M. Innocentini, J.R. Coury, Development of a double-layered ceramic filter for aerosol filtration at high-temperatures: the filter collection efficiency, Journal of Hazardous Materials 136 (2006) 747–756.
[6] G. Ahmadi, D.H. Smith, Gas flow and particle deposition in the hot-gas filter vessel of the Pinon Pine Project, Powder Technology 128 (2002) 1–10.
[7] K. Li, Ceramic Membranes for Separation and Reaction, John Wiley & Sons Ltd., Chichester, 2007.
[8] M.D.M. Innocentini, Aerosol filtration at high temperatures, Doctorate Thesis, Federal University of São Carlos, Brazil, 1997 (in Portuguese).
[9] J.P.K. Seville, S. Ivatl, G.K. Burnard, Recent advances in particulate removal from hot process gases, in: E. Schmidt (Ed.), High Temperature Gas Cleaning, vol. 1, Karlsruhe, 1996, pp. 3–25.
[10] Y. Kinemuchi, T. Suzuki, W. Jiang, K. Yatsui, Ceramic membrane filter using ultrafine powders, Journal of the American Ceramic Society 84 (2001) 2144–2146.
[11] S. Barg, C. Soltmann, M. Andrade, D. Koch, G. Grathwohl, Cellular ceramics by direct foaming of emulsified ceramic powder suspensions, Journal of the American Ceramic Society 91 (2008) 2823–2829.
[12] S. Barg, E.G. Moraes, D. Koch, G. Grathwohl, New cellular ceramics from high alkane phase emulsified suspensions (HAPES), Journal of the European Ceramic Society 29 (2009) 2439–2446.
[13] S. Barg, D. Koch, G. Grathwohl, Processing and properties of graded ceramic filters, Journal of the American Ceramic Society 92 (2009) 2854–2860.
[14] S. Barg, C. Soltmann, D. Koch, Verfahren zur herstellung offenporöser, anorganischer bauteile und verfahren zur herstellung offenporöser, anorganischer bauteile mit geschlossener Porosität in der äußeren Schicht, 2010. DE 102008058417.
[15] J. Hüppmeier, S. Barg, M. Baune, D. Koch, G. Grathwohl, J. Thöming, Oxygen feed membranes in autothermal steam-reformers – a robust temperature control, Fuel 89 (2010) 1257–1264.
[16] E.M.M. Ewais, S. Barg, G. Grathwohl, A.A. Garamoon, A. Samir, Processing of open porous zirconia via alkane phase emulsified suspensions for plasma applications, International Journal of Applied Ceramic Technology 8 (2011) 85–93.
[17] S. Barg, C. Soltmann, A. Schwab, D. Koch, W. Schwieger, G. Grathwohl, Novel open cell aluminum foams and their use as reactive support for zeolite crystallization, Journal of Porous Materials 18 (2011) 89–98.
[18] M.D.M. Innocentini, R.K. Faleiros, R. Pisani Jr., I. Thijs, J. Luyten, S. Mullens, Permeability of porous gelcast scaffolds for bone tissue engineering, Journal of Porous Materials 17 (2010) 615–627.
[19] J. Benitez, Principles and Modem Applications of Mass Transfer Operations, second ed., John Wiley & Sons, 2009.
[20] J.R. Welty, Fundamentals of Momentum Heat and Mass Transfer, Wiley, New York, 1984.
[21] A.E. Scheidegger, The Physics of Flow Through Porous Media, third ed., University of Toronto Press, 1974.
[22] E.A. Moreira, M.D.M. Innocentini, J.R. Coury, Permeability of ceramic foams to compressible and incompressible flow, Journal of the European Ceramic Society 24 (2004) 3209–3218.
[23] M.D.M. Innocentini, P. Sepulveda, F. Ortega, Permeability, in: M. Scheffler, P. Colombo (Eds.), Cellular Ceramics: Structure, Manufacturing, Properties and Applications, Wiley-VCH, Weinheim, 2005, pp. 313–340.
[24] M.D.M. Innocentini, P. Sepulveda, V.R. Salvini, J.R. Coury, V.C. Pandolfelli, Permeability and structure of cellular ceramics: a comparison between two preparation techniques, Journal of the American Ceramic Society 81 (1998) 3349–3352.
[25] D. Hlushkou, U. Tallarek, Transition from creeping via viscous-inertial to turbulent flow in fixed beds, Journal of Chromatography A 1126 (2006) 70–85.
[26] P. Moldrup, T. Olesen, T. Komatsu, P. Schjønning, D.E. Rolston, Tortuosity, diffusivity and permeability in the soil, liquid and gaseous phases, Soil Science Society of America Journal 65 (2001) 613–623.
[27] M.D.M Innocentini, M.G. Silva, B.A. Menegazzo, V.C. Pandolfelli, Permeability of refractory castables at high-temperatures, Journal of the American Ceramic Society 84 (2001) 645–647.
[28] M.D.M. Innocentini, A.R. Studart, R.G. Pileggi, V.C. Pandolfelli, PSD effect on the permeability of refractory castables, American Ceramic Society Bulletin 80 (2001) 31–36.
[29] M.D.M. Innocentini, F.T. Ramal Jr., R.G. Pileggi, V.C. Pandolfelli, Permeability and drying behavior of PSD-designed refractory castables, American Ceramic Society Bulletin 82 (2003) 1–6.
[30] S.H. Lee, Y.M. Jo, Application of Kozeny constant to a thin ceramic filter for hot gas cleaning, Industrial and Engineering Chemistry Research 8 (6) (2002) 552–556.
[31] D.W. Green, R.H. Perry, Perry's Chemical Engineers' Handbook, eighth ed., McGraw-Hill, 2008 (Sections 5–6).
[32] Y.M. Jo, R.B. Hutchison, J.A. Raper, Characterization of ceramic composite membrane filters for hot gas cleaning, Powder Technology 91 (1997) 55–62.
[33] M. Lupión, F.J. Gutiérrez Ortiz, B. Navarrete, V.J. Cortés, Assessment performance of high-temperature filtering elements, Fuel 89 (2010) 848–854.